Nanoanalytical Electron Microscopy Reveals A Sequential Mineralization Process Involving Carbonate-Containing Amorphous Precursors

Kharissa Nitiputri[1,2,3], Quentin M. Ramasse[4], Hélène Autefage[1,2,3], Catriona M. McGilvery[1], Suwimon Boonrungsiman[1,2,3]†, Nicholas D. Evans[5], Molly M. Stevens[1,2,3], Alexandra E. Porter[1*]*

[1]Department of Materials, [2]Department of Bioengineering, [3]Institute of Biomedical Engineering, Imperial College London, London SW7 2AZ UK, [4]SuperSTEM Laboratory, SciTech Daresbury Campus, Daresbury, WA4 4AD, and [5]Department of Bioengineering and Institute for Life Sciences, University of Southampton, Southampton, SO17 1BJ

Supplementary information

Supplementary Materials and Methods

Mouse neonatal osteoblast isolation and culture

Cell culture protocols were as previously described.[1,2] Briefly, osteoblasts were derived from two-day old neonatal CD-1 mice. The mice were sacrificed by cervical dislocation according to Imperial College London ethical guidelines. Calvarial tissue from all of the pups in a litter were removed and pooled, washed in phosphate-buffered solution (PBS), and removed from all soft tissue. The calvaria were then minced with sterile scissors. The minced calvaria were digested in a 1 mg/mL collagenase (Sigma) in Hank's Balanced Salt Solution (Invitrogen) with 10% (v/v) solution of 0.05% (wt/v) trypsin/EDTA (Invitrogen). Four digestions (20 minutes each) were followed by a fifth digestion (2 hours). Cells were collected by centrifugation of the last three supernatants. Cells were then plated in α-minimum essential medium (αMEM) (Invitrogen) supplemented with 15% (v/v) fetal bovine serum (FBS) (Invitrogen) and 1% (v/v) penicillin/streptomycin (P/S) (Invitrogen). The cells were cultured in an incubator under humidified atmosphere and 5% CO_2. It is notable that cell culture media are specifically formulated to replicate the partial pressure of CO_2 in arterial blood (4 – 6 kPa), when kept at this 5% CO_2 level in an incubator, and to buffer against changes in H^+. Cells from the third or fourth passage were used for experiments. To induce mineralization, 30,000 cells/cm^2 were seeded on glass cover slips and incubated for 28 days in αMEM supplemented with 15% (v/v) FBS, 1% (v/v) P/S, 50 μg/mL ascorbic acid, and 10 mM ß-glycerophosphate using a well-established mineralization protocol.[1,2] Dexamethasone (1 μM) was added to the culture from day 14 of the experiment. Experiments were conducted using 3 replicate experiments.

Preparation of Cells for TEM

An anhydrous sample preparation procedure previously described by Landis *et al.* was used to prepare the samples.[3] The samples were rinsed with PBS twice and then immersed in anhydrous ethylene glycol (Sigma) for three hours at room temperature. The samples were then immersed in fresh, dry acetonitrile three times for ten minutes each (*i.e.* a total of 30 minutes in acetonitrile). The samples were infiltrated with a Quetol-based resin as previously described.[1,2] TEM samples were sectioned to ~70 nm thickness using a Leica Ultramicrotome (Leica) and were immediately placed on 300 mesh copper lacey-carbon grids (Electron Microscopy Sciences). Selected sections were stained using uranyl acetate (Electron Microscopy Sciences) and lead citrate (Sigma-Aldrich) to enhance the organic or cellular contrast for imaging only (Figure 1A only). This preparation protocol does not crosslink proteins and so the structure of the organic components (*i.e.* the collagen and cell organelles) is only weakly preserved.[2,3]

Potential artefacts caused by the sample preparation

For the purpose of this study, samples were prepared by an anhydrous route to retain the crystallinity of the mineral at its earliest stages: Amorphous calcium phosphate is thermodynamically unstable in aqueous environments and quickly converts to a more stable, crystalline phase of hydroxyapatite.[4] Utilization of an anhydrous method avoids aqueous solution-induced mineral phase transformations and preserves the crystallinity of the bone apatite. We were confident that this method is the best method available for preserving the crystallinity, morphology and chemistry of the dominant CaP structures, as these structures have been seen in samples prepared by both this anhydrous sample preparation route and HPF/FS conducted in our previous work (Figure S7).[2] Anhydrous preparation routes are less

sophisticated than freezing routes; nevertheless, they are well established methods for preserving the chemistry, crystallinity and structure of CaP in tissues. For example, a modified version of the method used in our paper has been reported on in recent literature which maps the chemistry and structure of natural CaP nanoparticles in the intestine.[5] In addition, this anhydrous method allows the mineral to be easily visualised in a tissue background as it avoids the use of heavy-metal contrast agents (*e.g.* uranyl acetate and lead citrate) leaving sections unstained.

Each stage of the sample preparation protocol is described below to consider whether and which artefacts could arise:

Rinse with PBS: It is unlikely that calcium phosphate will precipitate when the sample is rinsed with PBS, as the cell culture medium (MEM) is already saturated in salts containing phosphates; the osmolarity of PBS and MEM cell culture medium are also matched.

Dehydration step: Moving from a hydrated to a dehydrated state (ethylene glycol and ethanol) could reduce the size of the CaP and induce crystallization of the surface of the amorphous CaP. Removing coordinated waters can lead to the crystallization of calcium carbonate/ calcium phosphate. Therefore, the crystallinity on the surface of the granules seen in figure S4 could be an artefact. However, the dehydration step should not alter the elemental composition, cause redistribution of ions or introduce carbonate. As the dehydration step cannot be avoided using the current TEM sample preparation protocol, we used a stronger dehydrating agent, *i.e.* ethylene glycol, to shorten the dehydration time required, thereby minimizing the likelihood of formation and growth of any new crystals. Ethylene glycol ($HO\text{-}CH_2\text{-}CH_2\text{-}OH$) has two hydroxyl groups, which can attract and hold water molecules more strongly, hence can offer a faster dehydration speed.

Cutting the thin TEM sections onto a water bath: The surface of the dense granules could crystallize, as the TEM sections were cut onto a water bath. The size of the granules is the same size range as the thickness of the sample, so the exposed faces of the granule will have been exposed to water (for ~5 seconds before they are collected onto a TEM grid and dried).

Preparation of Carbonated Hydroxyapatite Standard

A standard carbonated hydroxyapatite (CHA) sample (provided by Professor Serena Best, University of Cambridge) was used as a reference for the EELS spectra and to calculate the K factor for EDX analysis. The CHA was produced *via* a sodium free wet chemical precipitation reaction first described by Gibson & Bonfield.[6] CO_2 was bubbled through deionized water into the $Ca(OH)_2$ solution until the pH dropped to around 4. Aqueous H_3PO_4 (85 v/v % Fisher Scientific) was then added a rate of 5 mL/min. No pH control was necessary as the pH remained above 10.5. The sample was then prepared for TEM by suspending it in ethanol. The CHA was then sonicated, pipetted onto a carbon-coated TEM grid with excess solution removed using filter paper.

Electron Microscopy Imaging and Analysis

All TEM observations were made after viewing multiple regions from at least three separate cell cultures, and all of the minerals analyzed in this study were extracellular. Preliminary bright-field TEM imaging was performed on a JEOL 2000FX operated at 80 kV. An objective aperture was used to enhance contrast and reduce sample tearing due to charging effects. A JEOL 2100F operated at 200 kV was used for Scanning Transmission Electron Microscopy (STEM) imaging and energy dispersive X-ray spectroscopy (EDX) (Oxford Instruments IncaEnergy).

In STEM mode the electron beam is condensed down to a sub-nanometer probe and rastered across the sample to build up an image, with the signal collected on an annular detector. The signal that is collected at high angles (>50 mrad, known as High Angle Annular Dark Field, HAADF, imaging) is sensitive to the atomic number of the material and the thickness of the region being studied. In this way, regions with higher atomic number appear brighter in the image. Combining this method with analytical capabilities such as EDX and Electron Energy Loss Spectroscopy (EELS), chemical information can be achieved on the nanometer scale.

STEM imaging combined with EELS was performed on a Nion UltraSTEM™ (SuperSTEM, Daresbury, UK) at 100 kV with a probe convergence semi-angle of 32 mrad. The collection semi-angle into the spectrometer was 36 mrad and the HAADF detector collected electrons scattered by 79-195 mrad (semi-angle). The electron beam can be controlled to collect an EEL spectrum from each point on a sample (a spectrum image, SI), and analyzed to produce a chemical map. To ensure that edges from all elements of interest were collected, EELS spectrum images were collected with an energy dispersion of 0.5 eV/channel. The sample area had a relative thickness <0.5 (relative thickness t/λ, where λ is the electronic mean inelastic free path of the electron in the sample, and t the thickness of the sample). Supplementary EEL spectra and electron beam damage experiments were conducted on an FEI TITAN 80/300 (S)TEM operated at 80 kV (Imperial College London).

EELS Analysis

Gatan DigitalMicrograph software was used for STEM image and EELS analysis. The energy scale was calibrated to the onset of the carbon K-edge for amorphous carbon at 284.5 eV, found ubiquitously on the sample in regions containing only resin and thus providing a consistent internal energy scale reference. For each of the elemental edges (C, Ca, N, O, Si

and P), background subtraction was carried out using a power law model. A carbonated HA (CHA) standard was used to obtain reference spectra and identify phosphorus, carbon, calcium, nitrogen, and oxygen peaks.[7,8] Principal Component Analysis (PCA) was carried out using Hyperspy software to smooth the spectral data sets.[9,10]

Specifically for the carbon K edge, multi-Gaussian fitting was applied to further identify the signal's fine features contributed by different carbon bindings (as listed in Table S2). A typical example of such a multi-Gaussian fit is shown in Figure S7, with contributions from all components identified in Table S1. Maps of the relative strength of functional groups of interest (carbonyl and carbonate) across the spectrum images can then be generated by normalizing the amplitude of the corresponding Gaussian to that of the σ* peak, which is systematically present as the dominant feature characteristic of amorphous carbon.

Electron Dose for EELS experiments and Mineral Crystallinity

Biological samples are prone to electron beam induced damage. If not accounted for, this can lead to incorrect conclusions about experimental data. It is therefore important to establish that no damage has occurred in the specimen.

To confirm that no damage had occurred during the STEM-EELS experiments, an EELS damage experiment was conducted at the SuperSTEM. Previous work by our group has shown that a prominent and sharp peak at 530 eV in the oxygen K edge of these materials is only present once the sample has damaged (Peak X in Figure S6).[11] That study showed that in STEM 10^4 electrons/nm^2 is the threshold dose rate before the onset of damage can be detected, and hence EELS acquisition needs to be conducted using electron doses below this number to obtain reliable data. However, whilst electron dose can be used as a guide for when a sample damages, damage will vary depending on a number of factors, *e.g.* the nature of the sample and the vacuum levels in the microscope. For the samples reported on here, the

peak at 530 eV at the oxygen K edge is a good marker of early damage modifications of the sample's chemistry and, so long as the dose is kept below or close to this limit, it is assumed that little significant damage to the sample has occurred (this peak is induced by formation of O_2 oxygen molecules[12] or other forms of oxygen radicals, *e.g.* OH or CO).

In our study, initial damage experiments were conducted on sacrificial regions of the sample at various doses and dose-rates until the oxygen K edge damage peak was no longer present in the data. This provided a regime where the damage peak was not present but the signal was still high enough to interpret the fine structure of the elemental edges.

Fine structure in the Ca and P $L_{2,3}$ EELS edges

We saw no differences in fine structure in the calcium or phosphorous $L_{2,3}$ edges in the present study. Although the Ca L edge is known to present some fine structure variations depending on its bonding environment (although we note that most studies in the literature focus on XANES, rather than ELNES – where the spatial information is lost), the energy resolution necessary to fingerprint them is extremely high, and observing these differences also requires high signal to noise ratio. For practical reasons, both were difficult to achieve in the conditions used for this study where we tried to minimize the electron dose through a choice of a relatively low beam current, and a spectrometer dispersion set to a reasonably low value (thus obscuring the finest energy differences – to allow the simultaneous acquisition of all edges of interest). Similarly, fine structure differences in the P $L_{2,3}$ edge are known to be extremely subtle. As a result, we focused our analysis on the C K edge, whose fine structure is very sensitive to bonding changes even at the energy resolution achieved in this experiment, and for which the cross-section is high enough to allow reliable interpretation even at relatively low overall signal levels. Furthermore, the only difference in fine structure we saw between the dominant structures was the presence of the peak at 290eV, which can be

assigned to carbonate. Therefore we can deduce that it would not be possible to determine any difference in the phase of the mineral based on the Ca or P $L_{2,3}$ EELS signature.

The advent of ultra-high resolution beam monochromators for EELS may make further contributions along these lines possible: the rich fine structure of the Ca L edges known from XANES should be readily detectable with the energy resolution afforded by these new instruments (although the signal to noise requirements will remain a limiting factor) and we are certainly planning to apply these techniques in the future.

Supplementary Figures

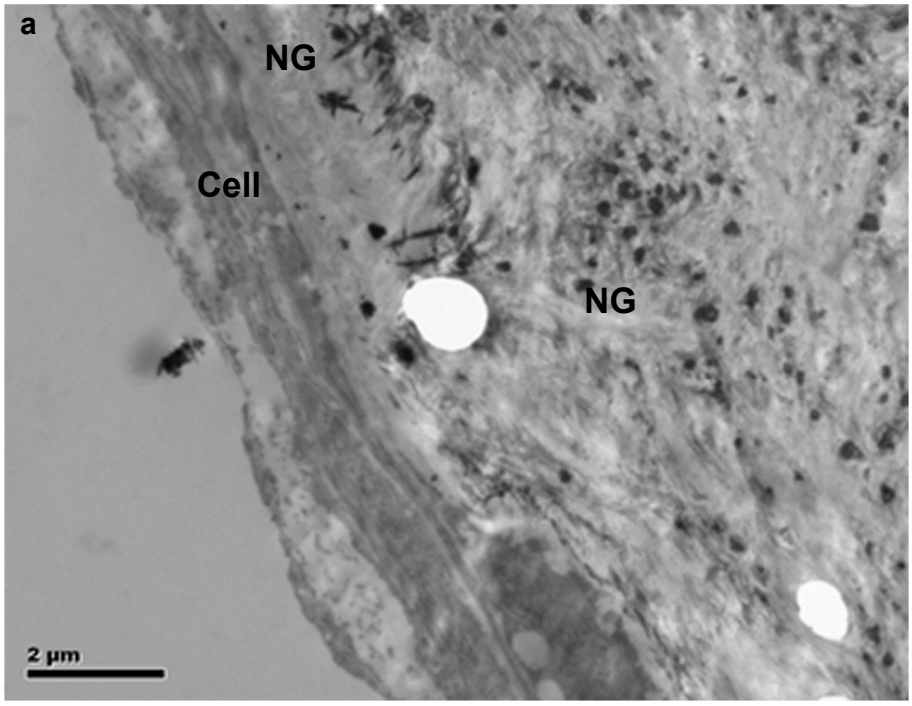

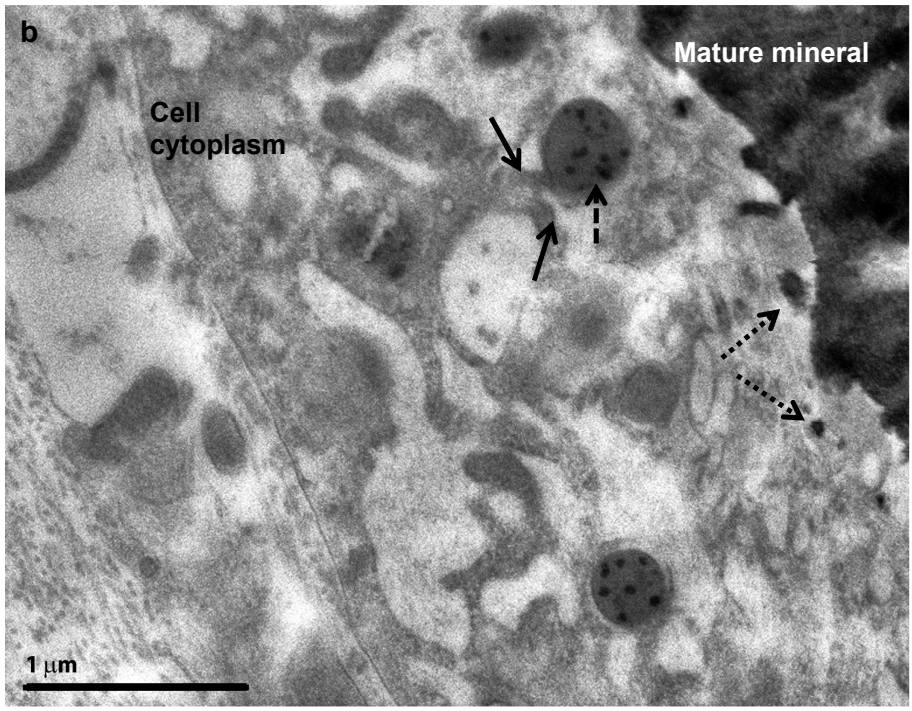

Figure S1. Spatial relationship between the osteoblast cells and the globular calcium phosphate aggregates comprised of needle-like crystals (NG), dense granules of apatite and the mature mineral crystals in the ECM. a) Anhydrously prepared cell showing NGs in the poorly mineralized ECM surrounding the cells. b) HPF/FS prepared cell prepared using methods described in ref (2). It is possible that the non-dotted arrows show membrane protrusions and that the dashed line points to a matrix vesicle containing dense granules of apatite at the plasma membrane of the cell; the NGs are outside the cell and close to the mineralized ECM (dotted arrows). However, the heavy metal stain is weak, so it is difficult to show conclusively using HPF/FS, where the dominant mineral structures lie in relation to the cells.

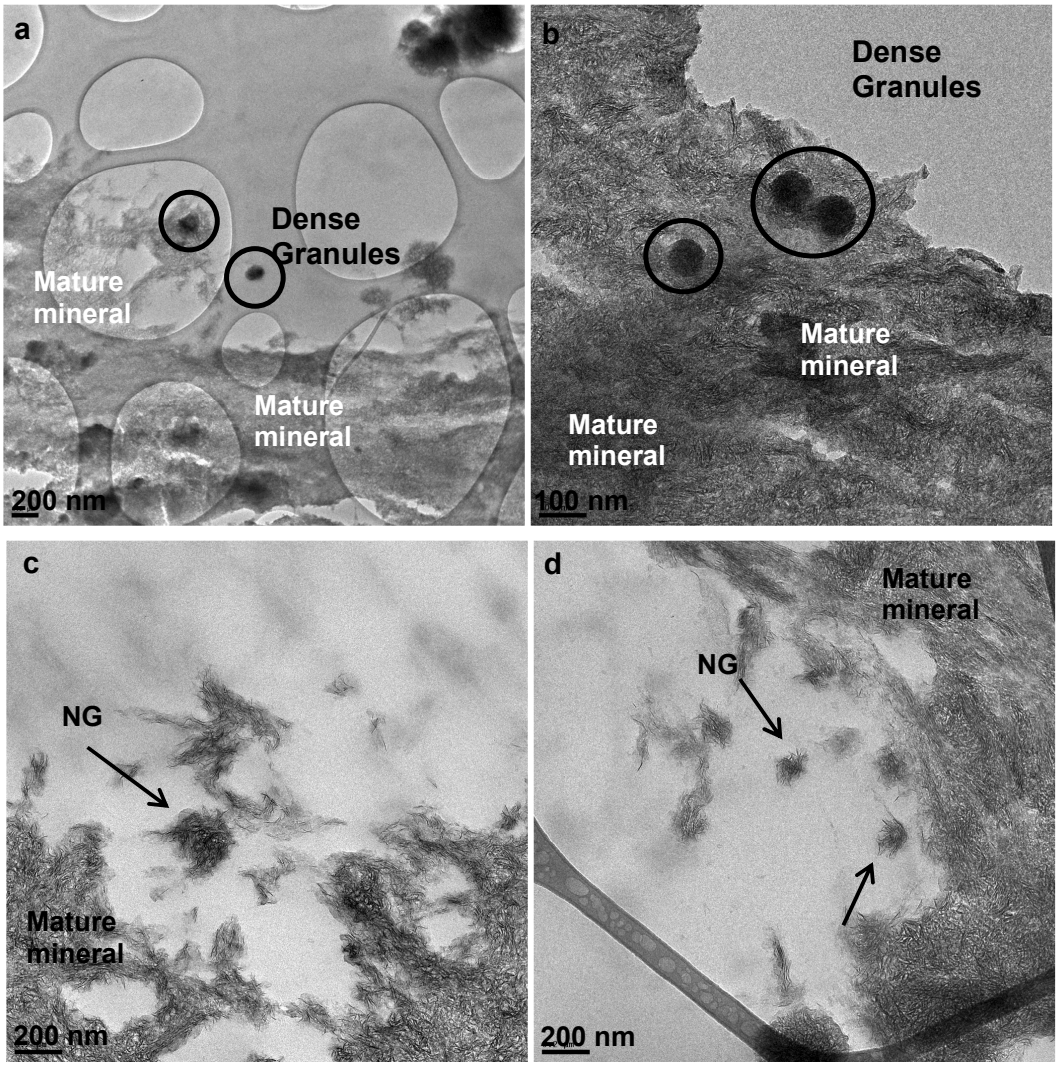

Figure S2. The spatial relationship between the dominant CaP structures and the mature mineralized extracellular matrix in unstained anhydrously prepared samples. The dense granules were found in close proximity to the plasma membrane of the cell (a), and in the mature mineralized extracellular matrix (b). The needle-like globules were always found outside the cells and adjacent to the mature mineralized extracellular matrix (c,d). Image (a) is taken on a holey carbon support film. NG-globular calcium phosphate aggregates.

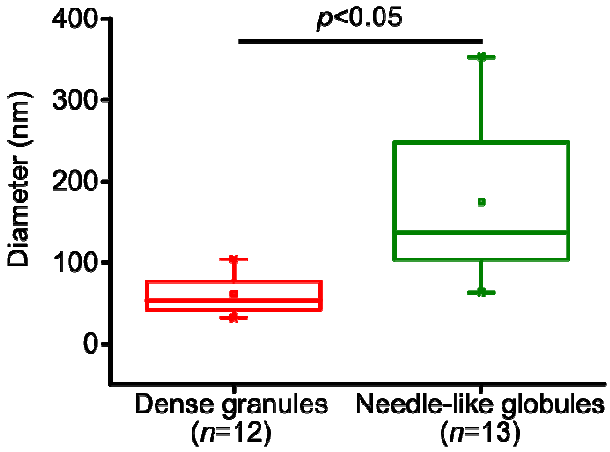

Figure S3. Size comparison between dense granules and needle-like calcium phosphate globules. Statistical significance was achieved ($p<0.05$) between the two groups. The average size of the dense globules and the needle-like globules were 61 nm and 175 nm, respectively. The maximum and minimum ranges of the values are denoted by the vertical lines above the box of the box plot. The end whiskers (horizontal line) of the box plot represent the 5th and 95th percentiles, which in this case is also coincides with the 1st and 99th percentiles denoted by ×. The box plot itself represents the 25th and 75th percentiles with the mean denoted by a small square in the box (□). The horizontal line going through the box represents the median of the data set.

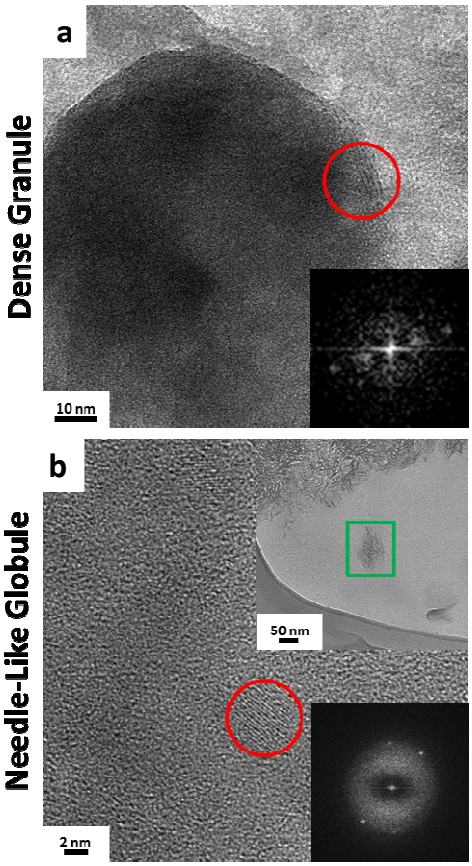

Figure S4. Crystallinity of the representative mineral morphologies. Phase contrast images with their respective Fourier transforms at right bottom corner of each images (taken from the whole image), showing the presence of lattice fringes (red circles) only on the surface of the dense granules, probably an artefact of sample preparation (a), the globular aggregates of apatite (b); inset shows low magnification image of the aggregate on the upper right hand corner of the image.

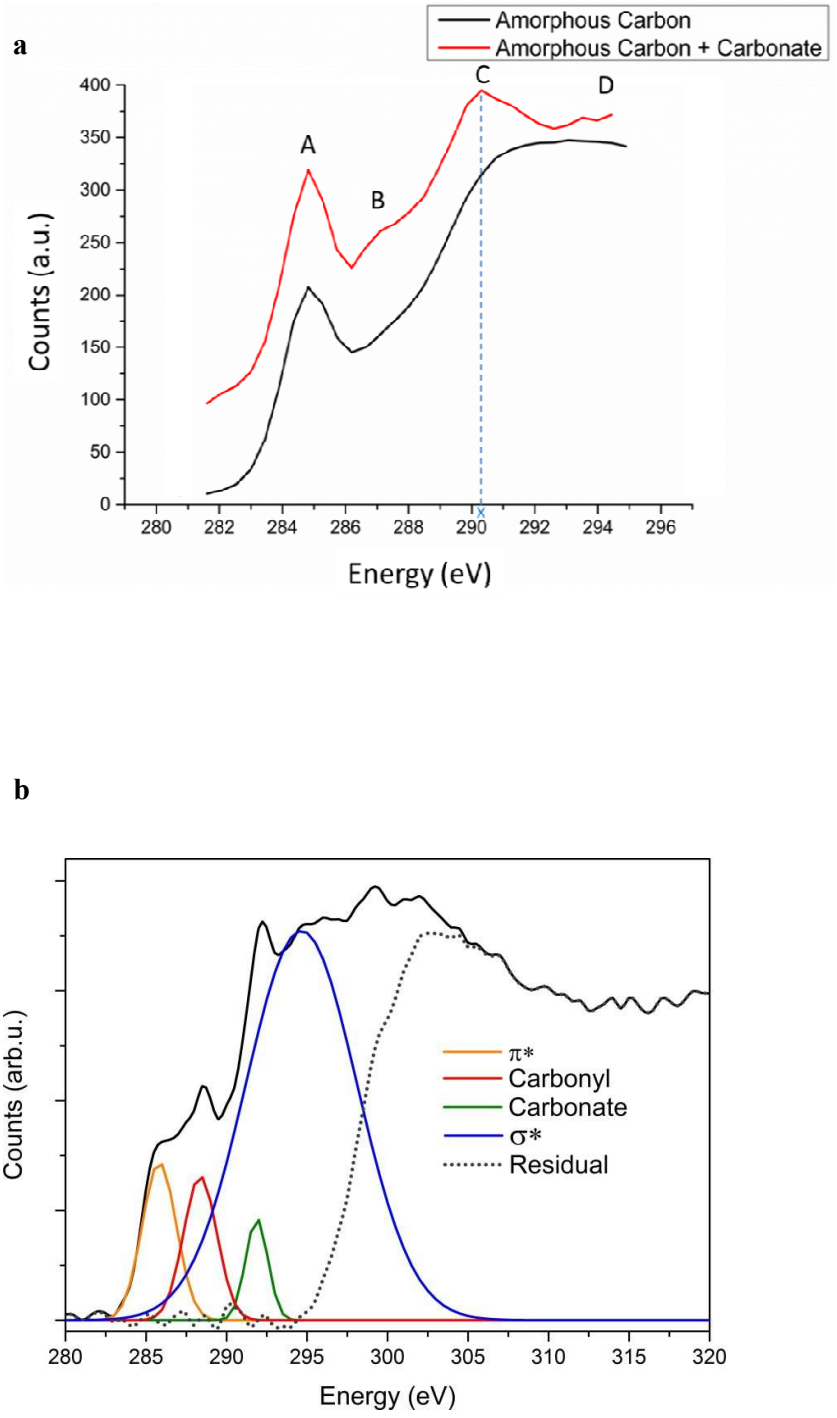

Figure S5. a) Standard curves used for MLLS fitting. The carbonate peak at the carbon K edge is present at 290.2 eV.[11,13] b) Gaussian fits used for figure 3.

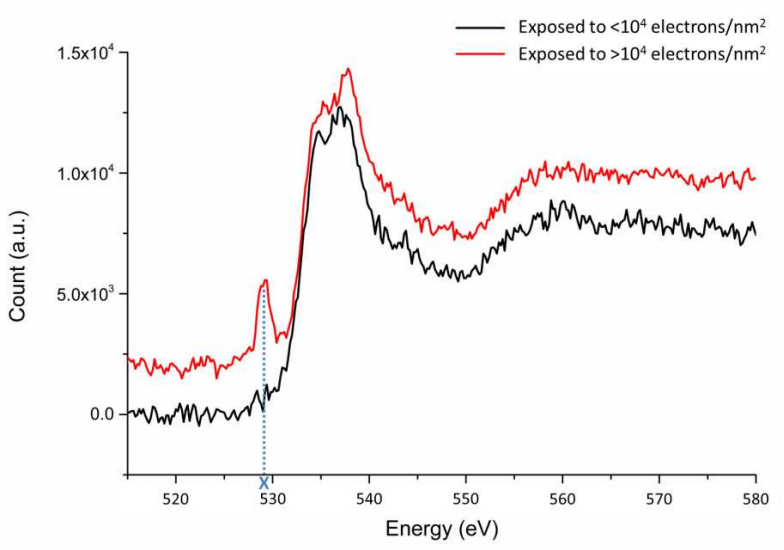

Figure S6. Damage markers seen in the oxygen K edge, in a CHA standard. The sample displays an additional peak at X just before 530 eV when exposed to an electron dose above 10^4 electrons/nm^2.

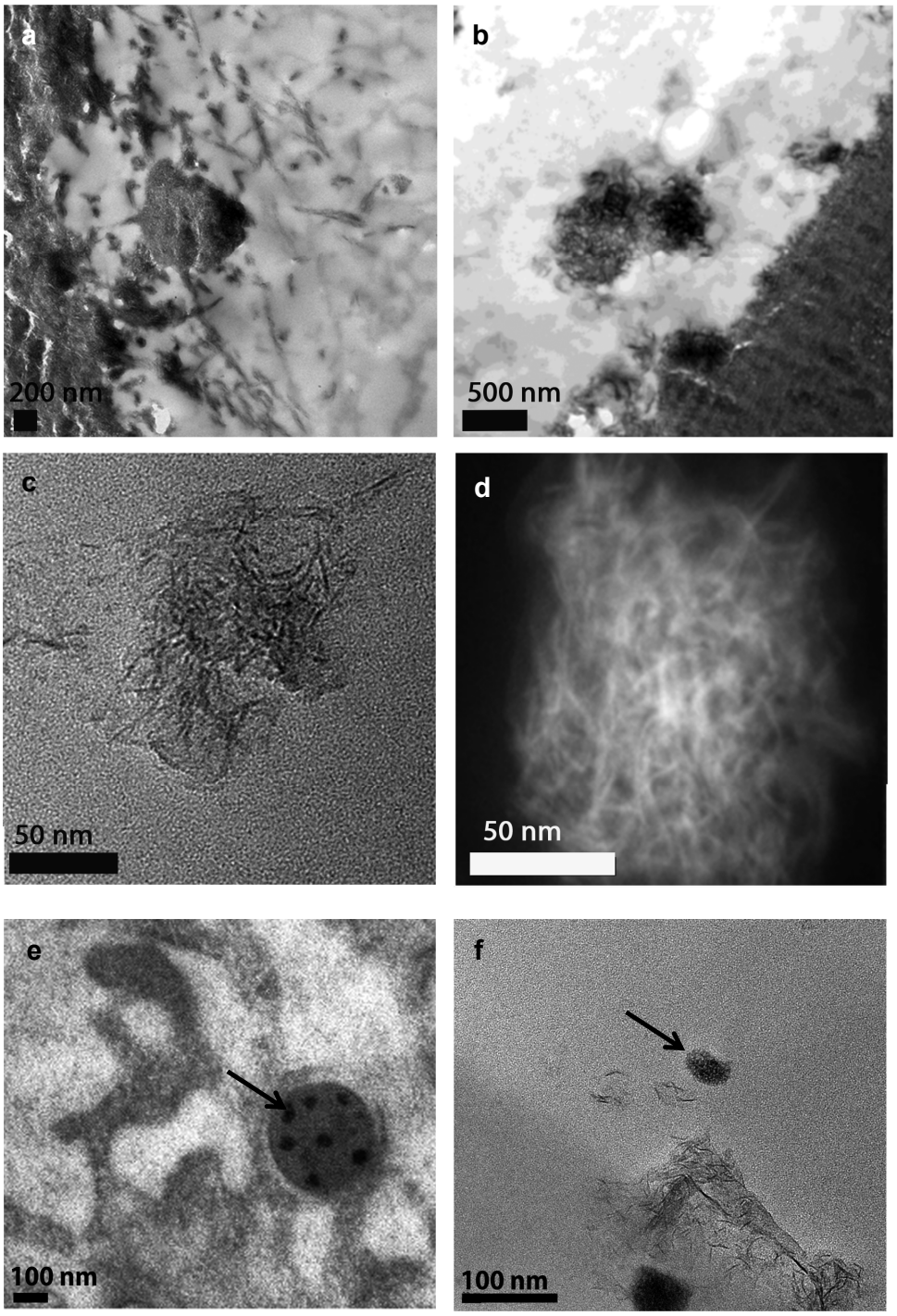

Figure S7. Comparison of the morphology of the dominant structures seen in samples prepared by HPF/FS[2] and anhydrous routes. Mature mineral crystals in the ECM (a,b) and globular calcium phosphate aggregate comprised of needle-like crystals (NG) (c,d). Dense

granules (arrows; c,f). Samples prepared by the anhydrous route (b,d,f) and by HPF/FS (a,c,e). d) HAADF-STEM image; the other images are bright field images.

Table S1. Approximate transitions in phosphorus $L_{2,3}$ edge, calcium $L_{2,3}$ edge, nitrogen K edge and oxygen K edge fine structure and assignments of peaks.

	Approximate Energy Loss (eV)	Description
Phosphorus		
A	138.0	Transitions to p-like states
B	141.0	Transitions from 2p state to new state created from due to interactions with calcium 3d orbital function (Characteristic for calcium-containing minerals)
C	146.0	Transitions to d-like states
D	160.0	Multiple scattering and the maximum 2p state cross section
Calcium		
E	348.0	Transitions from $L_3(2p_{3/2})$ to d-like states
F	351.0	Transitions from $L_2(2p_{1/2})$ to d-like states
Nitrogen		
G	400.0-401.0	1s-π* transitions; nitrogen in an aromatic ring, especially pyridine that is essential part of collagen crosslinking
H	408.0	Broad peak C is attributed more generally to 1s-σ* transitions in amino compounds
Oxygen		
I	537.0	Transitions to the vacant π* states of the Ca-O bonding environment
J	539.0	Transitions to the vacant σ* states of the Ca-O bonding environment
K	545.0	Transitions to 4s- and 4p-like states in calcium-oxygen bonds

Table S2. Approximate transitions in carbon K edge fine structure and assignments of peaks.

	Approximate Energy Loss (eV)	Bond assignments
Carbon		
A	284.5	Transitions to vacant π*states in in the carbon-carbon bonding environment (Amorphous Carbon) possibly from the embedding resin
B	287.0	Transitions to the vacant π*state of carbonyl groups possibly from amino acids.
C	290.2	Transitions to the vacant π*-A states of CO_3 groups
D	297.0	Transitions to vacant σ* states in the carbon-carbon bonding environment

Supplemental References

1. Gentleman, E.; Swain, R. J.; Evans, N. D.; Boonrungsiman, S.; Jell, G.; Ball, M. D.; Shean, T. A. V.; Oyen, M. L.; Porter, A.; Stevens, M. M.. Comparative Materials Differences Revealed in Engineered Bone as a Function of Cell-Specific Differentiation. *Nat. Mater.* **2009,** *8*, 763-770.

2. Boonrungsiman, S.; Gentleman, E.; Carzaniga, R.; Evans, N. D.; McComb, D. W.; Porter, A. E.; Stevens, M. M.. The Role of Intracellular Calcium Phosphate in Osteoblast-Mediated Bone Apatite Formation. *Proc. Natl. Acad. Sci. U. S. A.* **2012**, 109:14170-14175.

3. Landis, W. J.; Glimcher, M. J.. Electron Diffraction and Electron Probe Microanalysis of The Mineral Phase of Bone Tissue Prepared by Anhydrous Techniques. *J. Ultrastruc.Res.* **1978,** *63*, 188-223.

4. Boskey, A.L.; Posner, A.S.. Conversion of Amorphous Calcium Phosphate to Microcrystalline Hydroxyapatite–pH -Dependent, Solution-Mediated, Solid-Solid Conversion. *J. Phys. Chem.-Us.* **1973,** *77,* 2313–2317.

5. Powell, J. *et al.*. An Endogenous Nanomineral Chaperones Luminal Antigen and Peptidoglycan to Intestinal Immune Cells. *Nat Nanotechnol.* **2015** *10,*,361–369.

6. Gibson, I. R.; Bonfield, W.. Novel Synthesis and Characterization of an AB-Type Carbonate-Substituted Hydroxyapatite. *J.oBiomed. Mater. Res.* **2002,** *59*, 697-708.

7. Klosowski, M.. Electron Microscopy Characterisation of *In Vivo* Collagen and Mineral Ultrastructures, Their Development and Pathologies. Imperial College London, London, **2014**.

8. Garvie, L. A. J.. Can Electron Energy-Loss Spectroscopy (EELS) be Used to Quantify Hydrogen in Minerals from the O K edge? *Am. Mineral* **2010,** *95*, 92-97.

9. Hyperspy.

10. Arenal, R.; de la Peña, F.; Stéphan, O.; Walls, M.; Tencé, M.; Loiseau, A.; Colliex, C.. Extending the Analysis of EELS Spectrum-Imaging Data, from Elemental to Bond Mapping in Complex Nanostructures. *Ultramicroscopy* **2008,** *109*, 32-38.

11. Klosowski, M. M.; Friederichs, R. J.; Nichol, R.; Antolin, N.; Carzaniga, R.; Windl, W.; Best, S. M.; Shefelbine, S. J.; McComb, D. W.; Porter, A. E., Probing Carbonate in Bone Forming Minerals on the Nanometre Scale. *Acta Biomater* **2015,** *20,* 129-39.

12. Aronova, M. A.; Sousa, A. A.; Leapman, R. D.. EELS Characterization of Radiolytic Products in Frozen Samples. *Micron* **2011,** *42*, 252-256.

13. Brandes, J. A.; Wirick, S.; Jacobsen, C.. Carbon K-edge Spectra of Carbonate Minerals. *J. of Synchrotron Rad.* **2010,** *17,* 676-82.